ORIGINAL RESEARCH ARTICLE

Wear and Corrosion Resistant Eutectic High-Entropy Alloy Al$_{0.3}$CoCrFeNiMo$_{0.75}$ Produced by Laser Metal Deposition and Spark-Plasma Sintering

B. Preuß[1] · T. Lindner[1] · T. Uhlig[1] · T. Mehner[1] · G. Töberling[2] ·
G. Wagner[1] · T. Lampke[1]

Abstract Eutectic high-entropy alloys (EHEAs) with a fine-lamellar structure and homogenous property profile are of particular interest for wear and corrosion protection coatings. High cooling rates in the laser metal deposition (LMD) process can induce microstructure refinement and allow the formation of a supersaturated solid solution in EHEAs. A subsequent solution annealing can create the equilibrium state. In the present study, LMD coatings with an ultrafine-grained Widmanstätten structure were produced from the EHEA Al$_{0.3}$CoCrFeNiMo$_{0.75}$ gas atomized powder. High cooling rates during deposition led to a supersaturated solid solution with face-centered cubic (FCC) structure. The LMD coating exhibits the highest average hardness of 734 HV0.5, which drops to approx. 200 HV0.5 due to an increased microstructural domain size after heat treatment. Under oscillating wear, the formation of oxidized wear debris promotes material removal in the heat-treated condition. Corrosion tests reveal a deterioration of the passivation behavior. LMD processes exhibit great potential to create supersaturated solid solutions with refined structure in EHEAs to enhance the property profile.

✉ B. Preuß
bianca.preuss@mb.tu-chemnitz.de

1 Institute of Materials Science and Engineering (IWW), Chemnitz University of Technology, Chemnitz, Germany

2 Fraunhofer Institute for Machine Tools and Forming Technology (IWU), Chemnitz, Germany

Introduction

Coating technologies enable the application of novel alloy concepts such as high-entropy alloys (HEAs) for surface functionalization used in extreme engineering environments (Ref 1). HEAs consist of five or more main alloying constituents with equi- or near-equiatomic ratios and molar fractions of each element between 5 and 35% (Ref 2). Eutectic high-entropy alloys (EHEAs) with a fine lamellar structure and a homogeneous property profile are promising candidates for surface protection applications. The potential of this alloy concept was first recognized in the EHEA AlCoCrFeNi$_{2.1}$ (Ref 3). Miao et al. (Ref 4) reported excellent hardness, tribological properties, and softening resistance for this EHEA. Furthermore, pronounced corrosion resistance was reported (Ref 5, 6). The microstructure can change depending on the cooling rates during the production process and heat treatment (Ref 7-9). High cooling rates in particular can induce metastable phase states or ultrafine microstructures. In steels, the formation of a Widmanstätten structure can be observed at high cooling rates (Ref 10). In contrast, a microstructural transformation to a dense Widmanstätten structure was

detected in the HEA $Al_{0.5}CoCrFe_{1.5}NiTi_{0.5}$ aged at 1200 °C, which caused a secondary hardening effect (Ref 11). Chen et al. (Ref 12) showed a solid-state phase transformation for the HEA $CrFeCoNiAl_{0.6}$ by varying the cooling conditions. This led to a microstructure refinement and a change in the property profile. The influence of cooling conditions during coating processes such as laser metal deposition (LMD) and heat treatment on the functional properties of a metastable EHEAs has not been considered so far.

The powder metallurgical process of sintering has proven to be suitable for the production of HEA and EHEA bulk materials. Especially spark-plasma sintering (SPS) allows a cost-effective and simple alternative to vacuum arc melting (Ref 13). Various HEAs and EHEAs have already been produced by SPS processes (Ref 14-17). Due to the low cooling rates, deviating microstructures from the cast state can be observed (Ref 18, 19). Increasing the sintering temperature, the microstructure of the EHEA $AlCoCrFeNi_{2.1}$ gradually varied from initial lamellar eutectic structure to massive eutectic structure (Ref 19).

The coating technology allows the processing of HEAs and EHEAs under fast cooling conditions. Therefore, differences in microstructure and properties compared to the cast state were observed (Ref 1). In a previous study, a single-phase, body-centered cubic (BCC) microstructure was detected in the EHEA $Al_{0.3}CrFeCoNiMo_{0.75}$ feedstock powder (Ref 20). These were also detected in the high-velocity oxy-fuel (HVOF) sprayed coating besides an FCC phase and an HCP phase. Due to lower cooling rates, the casting showed no BCC structure. Rymer et al. (Ref 21) demonstrated good high-temperature wear resistance for the metastable EHEA $Al_{0.3}CrFeCoNiMo_{0.75}$ HVOF coating. LMD represents a promising approach to induce metastable states with a unique property profile. LMD is characterized by a non-equilibrium solidification, high cooling rates and a large temperature gradient (Ref 22). Cooling rates of 10^3-10^4 K/s (Ref 23) are achieved by LMD and approx. 10^6 K/s (Ref 24) for high-speed LMD. Huang et al. (Ref 25) found a microstructure refinement in the EHEA $AlCoCrFeNi_{2.1}$ produced by LMD. Hence, an improvement in mechanical properties such as high strength while maintaining a high ductility was realized.

Furthermore, a microstructure modification and variation in mechanical properties were observed after heat treatment (Ref 7, 26, 27). A hardness decrease was detected for the HEA $AlCoCrFeNiTi_{0.5}$ (Ref 14) as well as for the EHEAs $Al_{0.3}CoCrFeNiNb_{0.5}$ (Ref 28) and $CoCrFeNiNb_{0.5}$ (Ref 7) after heat treatment. A reduction of the heat-treatment temperature led to an increase in hardness. Kafexhiu et al. (Ref 29) determined microstructure modifications after heat treating the as-cast state of the EHEA $AlCoCrFeNi_{2.1}$. John et al. (Ref 26) observed similar

results for the same EHEA in the sintered state. Hence, wear performance was influenced.

Besides wear resistance, another essential system property is corrosion resistance. Previous studies show a unique corrosion behavior, especially for HEAs containing Cr, Ni, and Mo, which is different from conventional alloy systems with similar composition (Ref 30). Chou et al. (Ref 31) showed an inconspicuous behavior of Mo-containing HEAs $Co_{1.5}CrFeNi_{1.5}Ti_{0.5}Mo_X$ against pitting corrosion in a 1 M NaCl electrolyte. Nevertheless, Cr-rich phases and thus areas depleted in Cr reduced the passivation performance. Using a 0.5 M H_2SO_4 electrolyte, a degradation of the corrosion resistance was detected for the HEAs $Co_{1.5}CrFeNi_{1.5}Ti_{0.5}Mo_X$ with increasing Mo content. This is caused by the hindered formation of a protective layer on the surface. In particular, the reaction tendency of Mo and Cr leads to Cr-depleted areas that are more susceptible to corrosion (Ref 31). In contrast, Löbel et al. (Ref 32) found increased corrosion resistance (0.05 M H_2SO_4 electrolyte) in the HEA $Al_{0.3}CoCrFeNiMo_{0.2}$ due to passivation compared to the Mo-free HEA.

The present study is devoted to the influence of different microstructures of the EHEA $Al_{0.3}CrFeCoNiMo_{0.75}$ on the corrosion and wear resistance. High cooling rates during solidification are achieved for inert gas atomization as well as LMD processing. The thermal load at SPS induces recrystallization processes within the powder. Heat-treatments allow the equilibrium state to be achieved.

Materials and Methods

In the present investigations, gas atomized powder of the EHEA $Al_{0.3}CoCrFeNiMo_{0.75}$ (Nanoval GmbH & Co. KG, Berlin, Germany) was used to produce bulk materials via SPS and coatings by LMD. A detailed characterization of the powder was conducted in a previous study (Ref 20). A high-speed laser metal deposition (HS-LMD) system consisting of a TRUMPF BEO D70 Optic with a prototype TRUMPF 7-ray nozzle and a TRUMPF TruDisk 6001 laser source was used to produce the coatings. Round blanks of EN 1.4301 with a thickness of 6 mm and a diameter of 100 mm were selected as substrate. At 1.5 mm above the substrate surface, the focus point was set. The spot size was approx. 2 mm. For continuous powder feeding during the deposition process, a plate feeder was used. The processing was controlled by the axial rotation of a conventional industrial robot. In Table 1, the processing parameters are listed.

Using an SPS KCE FCT-HP D 25-SI (FCT Systeme GmbH, Frankenblick, Germany), the feedstock powder was compacted to bulk materials. Tools consisting of two graphite punches, one graphite die, and two graphite cones

Table 1 HS-LMD process parameters

Power, W	4000
Path velocity, m s^{-1}	0.5
Trace offset, mm	0.3
Feed rate, g min^{-1}	31
Ar gas flow rate, L min^{-1}	12
Layer thickness, μm	Approx. 500

Table 2 Parameter of the heat treatment

Temperature, °C	1100
Duration, h	12
Pressure, Pa	$\leq 10^{-2}$
Heating Rate, K min^{-1}	10
cooling rate, K min^{-1}	$\sim$ 150 (until 300 °C)

Table 3 Parameter of the ball-on-disk and reciprocating wear test

Ball-on-disk		Reciprocating wear test	
Force, N	20	Force, N	26
Radius, mm	5	Frequency, Hz	40
Speed, RPM	96	Time, s	900
Cycles	15916	Amplitude, mm	0.5
Counter body	Al$_2$O$_3$	Counter body	Al$_2$O$_3$
Diameter, mm	6	Diameter, mm	10

Table 4 Parameter of the constant scratch test

Force, N	50; 100; 150; 200
Radius, μm	200
Speed, mm min^{-1}	2.5
Length, mm	5
Tip	Rockwell-C

were used. Between the powder, the punches, and the die, graphite foils with a thickness of 0.3 mm were inserted to separate the tools from the powder. To prevent reactions with the atmosphere, the recipient was flushed with argon and evacuated twice

(< 2 mbar). The consolidation was conducted at a temperature of 1050 °C and a holding time of 10 min under a pressure of 50 MPa. A cooling rate of approx. 150 K/min until 300 °C was realized by water cooling of the punches. The produced SPS bulk materials exhibit a diameter of 40 mm and a height of 10 mm. Heat treatment of the LMD coating and SPS bulk material was conducted in a vacuum furnace (Torvac 12 Mark IV). In a previous study (Ref 20), the solidification behavior of the EHEA Al$_{0.3}$CoCrFeNiMo$_{0.75}$ was determined. Based on the solidus temperature, the parameters were chosen for the solution annealing heat treatment (Table 2).

For the characterization of the microstructure, a scanning electron microscope (SEM) LEO 1455VP (Zeiss, Jena, Germany) equipped with a backscattered-electrons detector (BSD) was used. Therefore, cross-sections of the SPS bulk material and LMD coating were prepared using standard metallographic preparation techniques. The SEM accelerating voltage was 25 kV. The chemical composition was detected by an integrated energy-dispersive X-ray spectroscopy (EDS) system EDS GENESIS (EDAX, Mahwah, NJ, USA). Phase determination of the LMD coating and SPS bulk material was conducted by an X-ray diffraction (XRD) measurement using a D8 Discover diffractometer. A 1D LYNXEYE XE-T detector was applied. By using Co Kα radiation, a diffraction angle range between 20° and 130° was analyzed. A conversion of the diffraction angles according to the Cu Kα radiation was

carried out. The porosity of the LMD coatings and SPS bulk materials were evaluated by image analysis method with the software ImageJ. Microhardness measurements (Vickers hardness HV0.5) were conducted by a Wilson Tukon 1102 device (Buehler, Uzwil, Switzerland) on the cross-sections. The average value was calculated from ten individual Vickers indents with a load of 4.903 N applied for five seconds.

For the corrosion and wear tests, the SPS bulk material and LMD coatings were grinded (US#1200). The tribological wear behavior was analyzed under scratch load as well as under sliding and oscillating wear conditions. Each wear test was repeated three times. Ball-on-disk wear tests were conducted according to the ASTM G 99 standard. The wear volume and wear depth were detected using a 3D profilometer MikroCAD (GFMesstechnik GmbH, Teltow, Germany). A reciprocating wear test to detect the behavior under oscillating wear conditions was conducted according to the ASTM G 133 standard using a Wazau SVT 40 device (Wazau, Berlin, Germany). The wear track was evaluated by using the 3D profilometer. The test parameters are shown in Table 3. The scratch test parameters are listed in Table 4. A scratch tester CSM Revetest-RST (CSM Instruments, Massachusetts, United States of America) was used. The tests were conducted under constant loads. Furthermore, the same device served to determine the scratch depth. Three scratches were conducted for each load.

Investigations regarding the corrosion behavior were conducted using the SPS bulk materials (Table 5). The pitting resistance and the passivation behavior were detected by potentiodynamic polarization measurements with an electrochemical workstation ZENNIUM

Table 5 Parameter of the corrosion tests

Electrolyte	0.5 M NaCl	0.05 M H$_2$SO$_4$
Scan rate, mV s^{-1}	1	1
Polarization range	OCP − 150 mV to + 1300 mV (with current limit 20 mA)	OCP − 150 mV to + 1300 mV
Number of measurements	5	5
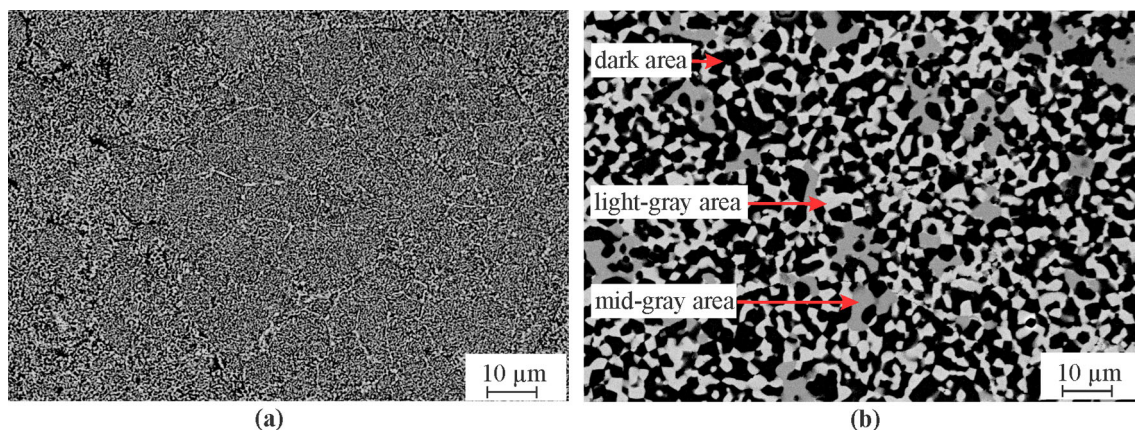
Fig. 1 SEM images (BSD) of the (a) untreated and (b) heat-treated SPS Al$_{0.3}$CoCrFeNiMo$_{0.75}$ bulk material

(ZAHNER-Elektrik GmbH & Co, Kronach, Germany). All tests have been carried out at room temperature with a three-electrode arrangement. A Pt sheet (20 × 20 mm^2) serves as counter electrode. A Ag/AgCl (saturated KCl) electrode was used as a reference electrode. The potentials were converted (conversion factor 197.6 mV) to reflect values vs. the standard hydrogen electrode (SHE). 10 mm of the sample surface were exposed to the electrolyte. The open-circuit potential (OCP) has been recorded for 15 min prior to each measurement. The parameters are shown in Table 5. The corrosion potential E_{corr} and the corrosion current density i_{corr} were determined by fitting the curves close to E_{corr} using the Butler-Volmer equation.

Results and Discussion

Microstructure, Phase Formation and Chemical Composition

Figure 1 shows SEM images of the Al$_{0.3}$CoCrFeNiMo$_{0.75}$ SPS bulk material in the untreated and heat-treated state. A heterogeneous microstructure was observed for both conditions. The contrast in the BSD allows for the distinction of different phases, i.e., the contrast is caused by differences in the chemical compositions of the phases. The brighter-appearing phases are rich in elements with higher atomic numbers. Based on the previous study (Ref 20), the dark phase shows an FCC structure and the bright phase an HCP structure.

Table 6 Chemical composition (at. %) determined by EDS of the SPS Al$_{0.3}$CoCrFeNiMo$_{0.75}$ bulk material in the untreated and heat-treated condition

State	Area	Al	Co	Cr	Fe	Ni	Mo
Nominal	Overall	5.9	19.8	19.8	19.8	19.8	14.9
Untreated	Overall	6.4	19.4	19.4	19.3	20.4	15.1
Heat-treated	Overall	5.9	20.2	20.0	20.4	20.1	13.4
	Light-gray area	2.9	19.3	22.3	18.4	11.9	25.2
	Mid-gray area	4.3	18.2	26.2	19.1	14.2	18.0
	Dark area	7.6	21.1	17.9	22.0	26.0	5.4

The FCC phase represents the solid solution, whereas the HCP phase is a intermetallic phase (Ref 33, 34). The untreated SPS bulk material (Fig. 1a) exhibits a fine eutectic structure. A high amount of bright phases along the grain boundaries was determined. After heat treatment (Fig. 1b), a microstructure coarsening was detected. Three different material contrasts can be recognized. Next to the light-gray phase (FCC) and dark phase (HCP), a mid-gray phase was detected. The SEM images showed only a few pores in the SPS bulk material. A porosity below 1 % was detected for both the untreated and heat-treated SPS bulk materials.

EDS measurements were conducted to detect the chemical composition of the SPS bulk material. The results are listed in Table 6. Only an area scan was carried out for the untreated SPS bulk material, because of the small microstructure domain size. Compared to the nominal
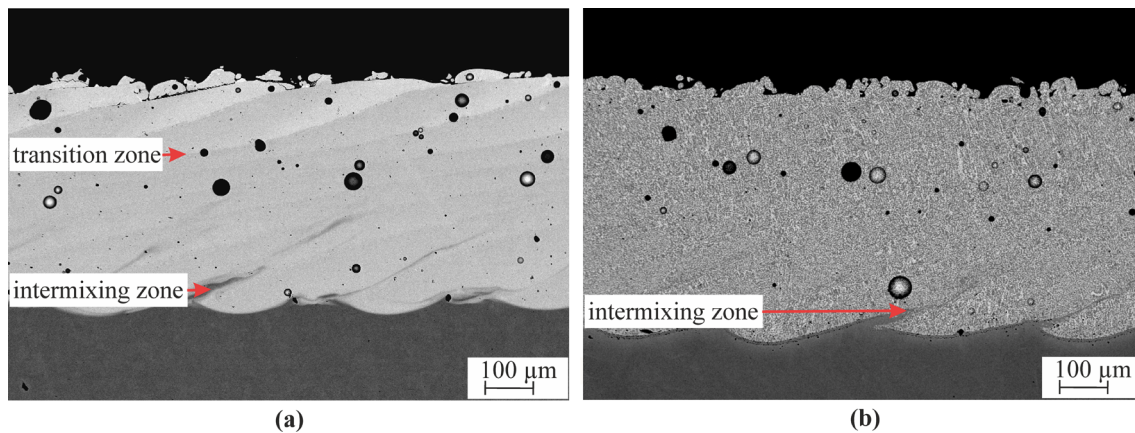
Fig. 2 SEM images (BSD) of the (a) untreated and (b) heat-treated LMD $Al_{0.3}CoCrFeNiMo_{0.75}$ coating (overview)

composition, the untreated and heat-treated conditions showed slight deviations in the chemical composition by observing the area-scan results. In the case of the heat-treated SPS bulk material, spot measurements of the individual areas were conducted. The light-gray area is Cr- and Mo-rich, whereas the dark area showed a higher Al, Co, Fe, and Ni contents. Hsu et al. (Ref 35) observed a similar tendency in the HEA $AlCoCrFeNiMo_{0.5}$, whereby the (Mo, Cr)-rich area represents the σ-phase. Hence, the solid solution in this EHEA primarily consists of Al, Co, Fe, and Ni. The mid-gray area shows a significantly higher Cr content and lower Mo content than the light-gray area. Similar to the mid-gray phase, Wu et al. (Ref 36) observed for the μ-phase a similar, extraordinarily high Cr content.

The microstructure of the LMD coatings (Fig. 2) was characterized in detail using SEM. In the overview images, Fig. 2(a) and (b), pores are visible for both the untreated and heat-treated LMD coating. A porosity of approx. 5% and a coating thickness of approx. 500 µm was measured. Due to the melt-metallurgical production, a closed porosity was realized. High residual stresses caused by fast cooling in the LMD process lead to cracking of the coating. The pores are preferentially located in the center and the top of the coatings. In Fig. 2(a), the offset during deposition of the LMD coating can be observed by transition zones arranged in angles of about 20°-40° to the substrate. The individual tracks have a plate-like shape. Due to the low heat input caused by the high coating speed, a wide and thin melt pool is formed (Ref 37). These transition zones are almost not visible in the heat-treated LMD coating. The material contrast indicates the segregation of three phases (Fig. 2b). The phase formation and eutectic structure is similar to those in the heat-treated SPS bulk material.

Detailed SEM images of the LMD coatings surface, center, and interface are shown in Fig. 3. An intermixing of the substrate material and the coating was observed in Fig. 3(a) and (b). These areas of intermixing can be seen

along the direction of feed at approx. 45°. A gray strip with a different material contrast to the bright phases in the LMD coating is formed parallel to the intermixed substrate. An accumulation of small precipitates was detected in the interface between the coating and substrate. These are more pronounced after the heat treatment. The stick-shaped dark precipitates are AlN compounds as determined by qualitative EDS measurements. These have formed during the LMD process by mixing the coating material with the N-containing substrate EN1.4301 (Ref 38). Their low formation enthalpy leads to diffusion-induced expansion during heat treatment. Figure 3(c) and (d) show the microstructure of the LMD coating center. The transition zone in the untreated LMD coating exhibits a coarser structure due to renewed melting during deposition. Between the transition zones, the microstructure is fine-grained and hardly recognizable. The predominantly elongated grains perpendicular to the transition zone create a directionally solidified structure. The grain boundaries are bright, indicating an enrichment with heavy elements such as Mo. The heat treatment necessitates the formation of a coarsened eutectic structure. Previously present strongly pronounced transition zones transform into barely visible bands with elongated-appearing phases by diffusion during heat treatment (Fig. 3d). The grain size decreases toward the coating surface (Fig. 3e) in the untreated LMD coating because of rapid solidification. Globular grain boundaries are formed. The near-surface microstructure in the heat-treated condition is similar to that of the coating center (Fig. 3f, d). A uniform arrangement of the microstructure due to the diffusion process during heat treatment is observed for the heat-treated LMD coating. Similar to the SPS bulk material, three different material contrasts are visible.

The transition zone in the untreated LMD coating was recorded with a higher magnification to more accurately capture the microstructure present (Fig. 4). Above the
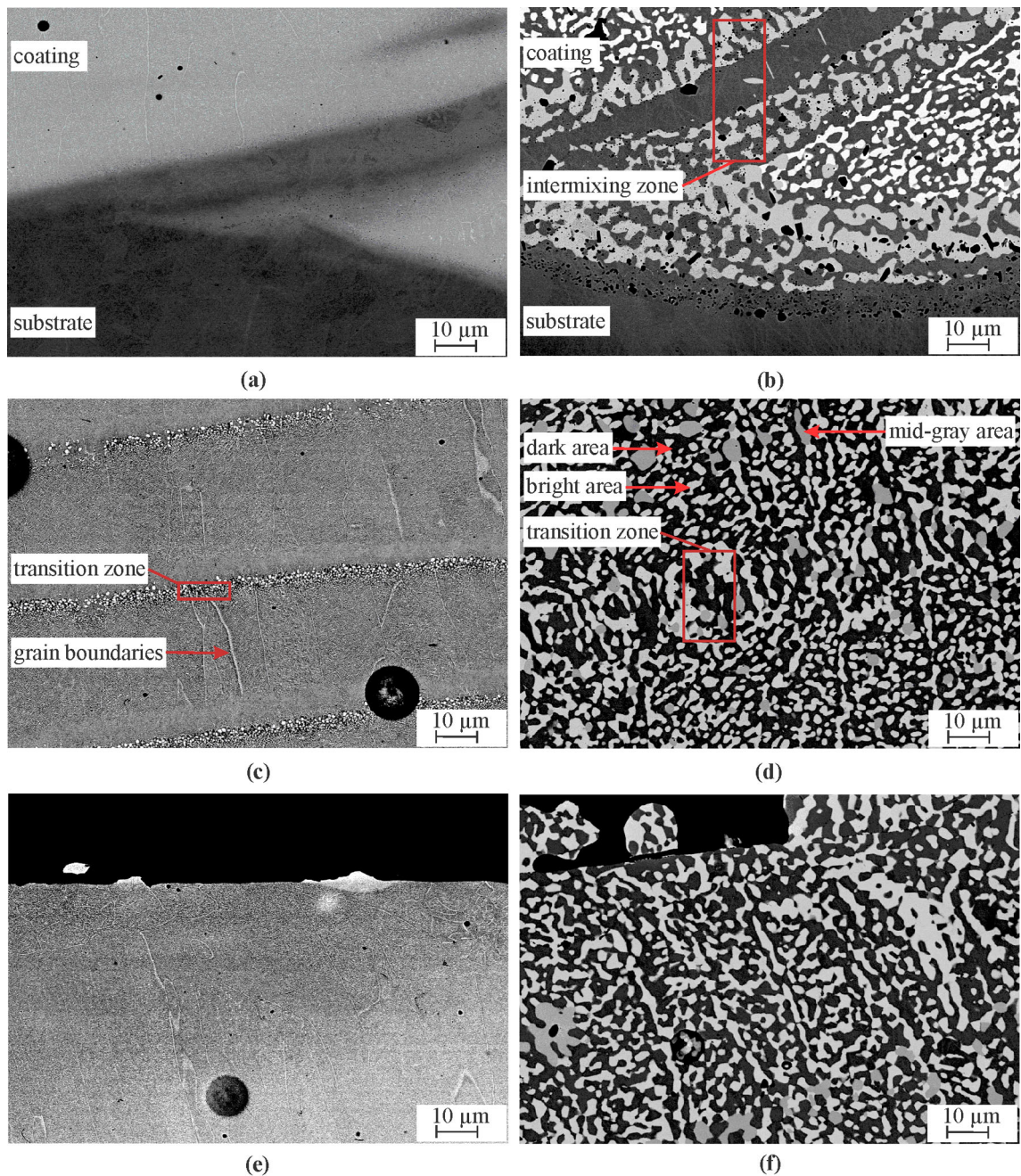
Fig. 3 SEM images (BSD) of the EHEA $Al_{0.3}CoCrFeNiMo_{0.75}$ untreated LMD (a) interface, (c) center of the coating, (e) surface; heat-treated LMD (b) interface, (d) center of the coating, (f) surface

repeatedly melted layer, ultrafine eutectic structures are visible. Within the bright-appearing grain boundaries, an needle-shaped microstructure was observed. These arrangements are often characterized as Widmanstätten structure (Ref 39), formed due to rapid cooling rates.

Table 7 summarizes the EDX values of the untreated and heat-treated LMD coatings. As for the SPS bulk materials, the chemical composition for both conditions detected by an area scan deviates only minimally from the nominal composition. A Cr-Mo-rich light-gray area and an Al-, Co-, Fe-, and Ni-rich dark area are present in the heat-treated LMD coating. The element concentrations in the areas deviate from the SPS bulk material. It was found that the Mo and Cr contents are significantly lower in the intermetallic phase and higher in the solid solution. The Ni content is also reduced in the solid solution, whereas the Al content is increased. The mid-gray area showed a higher Cr content compared to the light-gray and dark area. In

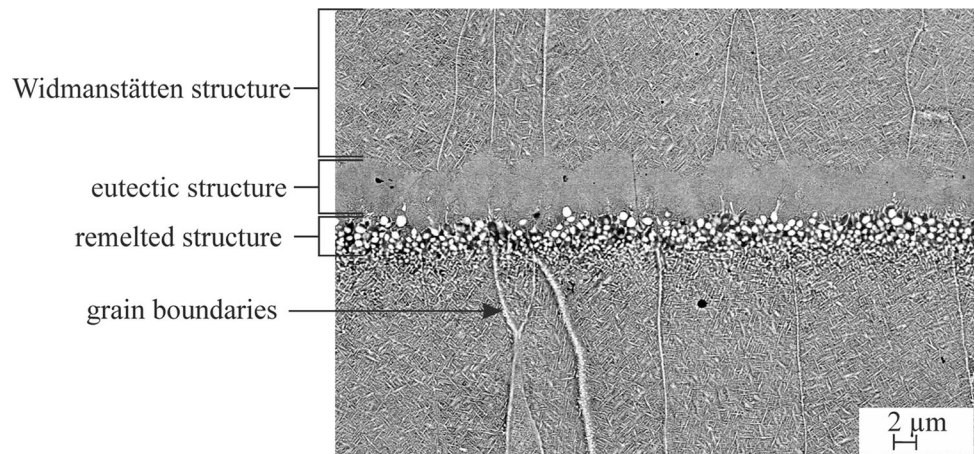Fig. 4 SEM images (BSD) of the LMD coating center in the untreated condition.

Table 7 Chemical composition (at. %) determined by EDS of the LMD $Al_{0.3}CoCrFeNiMo_{0.75}$ coating in the untreated and heat-treated condition

State	Area	Al	Co	Cr	Fe	Ni	Mo
Nominal	Overall	5.9	19.8	19.8	19.8	19.8	14.9
Untreated	Overall	5.7	19.9	19.9	20.6	20.1	13.8
Heat-treated	Overall	5.6	20.0	19.7	20.8	20.8	13.1
	Light-bright area	2.6	19.1	21.4	18.8	13.7	24.4
	Mid-gray area	3.1	18.2	28.1	19.1	12.1	19.4
	Dark area	8.3	20.6	18.3	21.8	24.2	6.8

contrast to the mid-gray area in the SPS bulk material, this area exhibits higher Cr and Mo contents in the LMD coating. Consequently, the preceding production process has a significant influence on the chemical composition despite additional homogenization.

The phase composition of the SPS bulk materials and LMD coatings was investigated by measuring their surface using XRD (Fig. 5). FCC (austenite structure, based on PDF 00-033-0397), HCP ($MoFe_2$ type, based on PDF 01-082-4709) and BCT (Ni-V type, based on PDF 01-081-7034) phases each with adjusted lattice parameters were detected in both the SPS bulk materials and the LMD coatings. The highest peak intensities are obtained in all conditions for the FCC phase. The solid solution is rich in Al, Co, Fe, and Ni. Surrounding the main peak of the FCC phase, peaks with lower intensity for the BCT phases were observed. Palguna et al. (Ref 40) determined also a BCT σ-phase in the HEA $Al_{0.5}CoCrFeNiMo_{0.5}$. This phase exhibits a higher Cr content than Mo content. Based on this previous study, the mid-gray area was assigned to the BCT σ-phase. The light-gray phase showed a higher Mo content than Cr content. Hence, this is the intermetallic μ-phase (Ref 33, 34, 36). In contrast to the study of Wu et al. (Ref 36), which reports a rhombohedral structure for the μ-phase, a HCP phase was detected for the μ-phase in this study. Rhombohedral structure and HCP are similar and cannot be distinguished reliably. A detailed examination of the diffractograms shows an increase in peak width for the
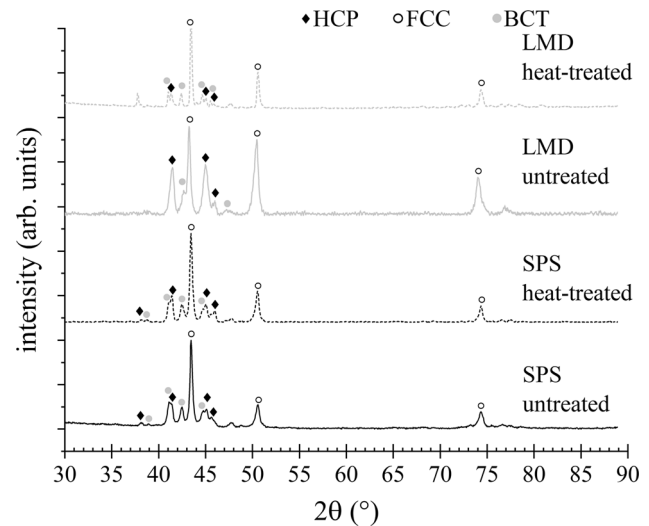

Fig. 5 Diffractograms of the $Al_{0.3}CoCrFeNiMo_{0.75}$ untreated and heat-treated SPS bulk material and LMD coating

untreated LMD coating. A higher defect density or lower crystallite size could be possible reasons. Furthermore, a pronounced peak shift to smaller angles was detected for the untreated LMD coating, indicating an increased lattice spacing in the FCC phase. This correlates with the higher cooling conditions during the LMD process. Hence, the diffusion is reduced. Higher Mo and Cr contents in the solid solution compared to the other conditions are present and lead to a lattice distortion. A texture ({200} lattice
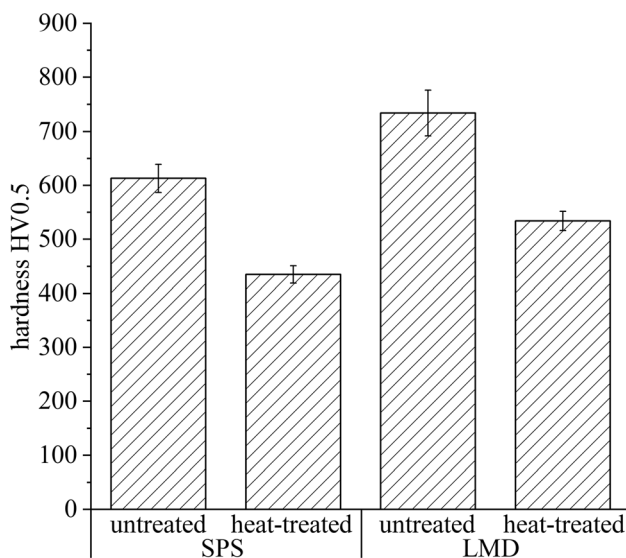
Fig. 6 Surface hardness HV0.5 of the SPS bulk material and LMD coating in the untreated and heat-treated states

planes at angles around 51° preferentially parallel to the surface) was detected for the untreated LMD coating. This can be explained by a preferential solidification direction (Fig. 4).

Hardness and Wear Resistance

In Fig. 6, the average microhardness is shown calculated from ten individual indents. The highest hardness was measured for the untreated LMD coating. This caused by the ultrafine-grained Widmanstätten structure (Ref 41) and the high solid-solution strengthening of the FCC (Ref 42). Due to microstructure coarsening and reduced solid solution strengthening, the hardness decreases significantly after the heat treatment. The lower proportion of phase boundaries leads to less hindrance of the dislocation movement. The differences between the heat-treated conditions are based on the altered chemical composition of the individual phases (Ref 43). This is contrary to the findings of a previous study on the EHEA $Al_{0.3-}CoCrFeNiNb_{0.5}$ (Ref 28). This EHEA exhibit similar hardness values after the heat treatment for the SPS and LMD states. Thus, a significant influence of the eutectoid transformation in the observed EHEA is perceptible.

Ball-on-disk tests were performed to investigate the resistance to sliding wear. The wear tracks were evaluated regarding the wear depth and wear rate (Fig. 7). The untreated SPS exhibits the highest wear resistance under sliding wear conditions, which is caused by low porosity, the balance between hard intermetallic HCP (Ref 33-35) and soft FCC phases, as well as a fine-eutectic structure. Furthermore, the worn surface shows delamination, wear

debris and ploughs (Fig. 8a). Compared to the other conditions with dominating abrasive wear, the main wear mechanism for the untreated SPS bulk material is surface fatigue. The higher wear rate of the untreated LMD coating is caused by the higher porosity and abrasive wear mechanism (Fig. 8c). The sliding wear resistance decreases due to the heat treatment for both conditions, which could be caused by the significantly lower hardness (Ref 44) compared to the untreated states. Furrows in the worn surface are present in the heat-treated conditions (Fig. 8b, d). The heat-treated SPS bulk material showed a lower wear rate but significantly higher wear depth than the heat-treated LMD coating. By comparing the wear area, the wear track of the heat-treated SPS bulk material exhibits an area of 0.018 ± 0.003 mm^2 and for the heat-treated LMD coating an area of 0.066 ± 0.014 mm^2 was recorded. The higher wear area and wear rate indicate wider wear tracks for the LMD coating. This may have led to the counter body being worn down more by the untreated LMD coating, resulting in a larger contact surface.

Figure 9 shows the wear depth and wear rate after the reciprocating wear test. The highest resistance to oscillating wear was determined for the untreated LMD coating. The higher hardness due to the ultrafine-grained Widmanstätten structure is the main reason. Furthermore, the untreated LMD coating shows the lowest proportion of wear debris on the worn surface (Fig. 10c). Dominant features are delamination and abrasion. Both surface fatigue and abrasive wear mechanisms are present. Similar wear mechanisms were detected for the untreated SPS bulk material. Rymer et al. (Ref 45) showed also a flake-like debris and grooves for the untreated EHEA LMD coating. Due to microstructure coarsening, the oscillating wear resistance decreases after the heat treatment. The proportion of wear debris increases significantly. These operate as an additional wear body between the surface and the counter body, creating deep grooves or plows (Ref 45). Thus, abrasion was identified as wear mechanism for the heat-treated states. BSD images of the wear surface in Fig. 11 showed a pronounced material contrast. Rymer et al. (Ref 45) also detected darker areas (wear debris) due to oxidation. Compared to the untreated LMD coating, the oxidized areas increase for the untreated SPS bulk material and the heat-treated conditions. As a result of the insufficient bonding of the oxidized areas, more wear debris are formed, which leads to higher material removal. Hence, tribo-oxidation can be deduced as a further wear mechanism.

For all conditions, comparisons of the wear resistance show a higher wear rate under oscillating wear than under sliding wear conditions. This difference is due to the higher numbers of cycles and the increased contact temperature during the reciprocating wear test. The contact temperature is influenced by the number of cycles with the applied load as well as frequency (Ref 46). The pronounced material

Fig. 7 Wear depth and wear rate (ball-on-disk test) of the SPS bulk material and LMD coating in the untreated and heat-treated state
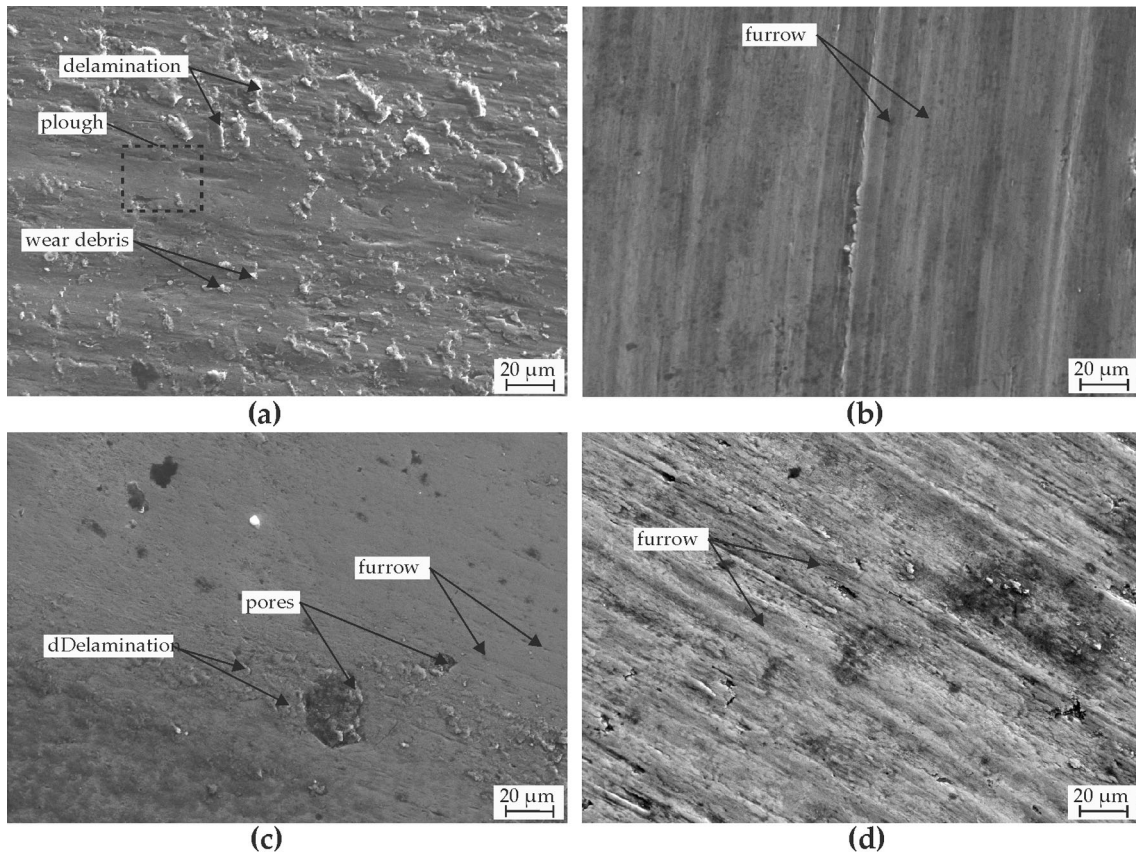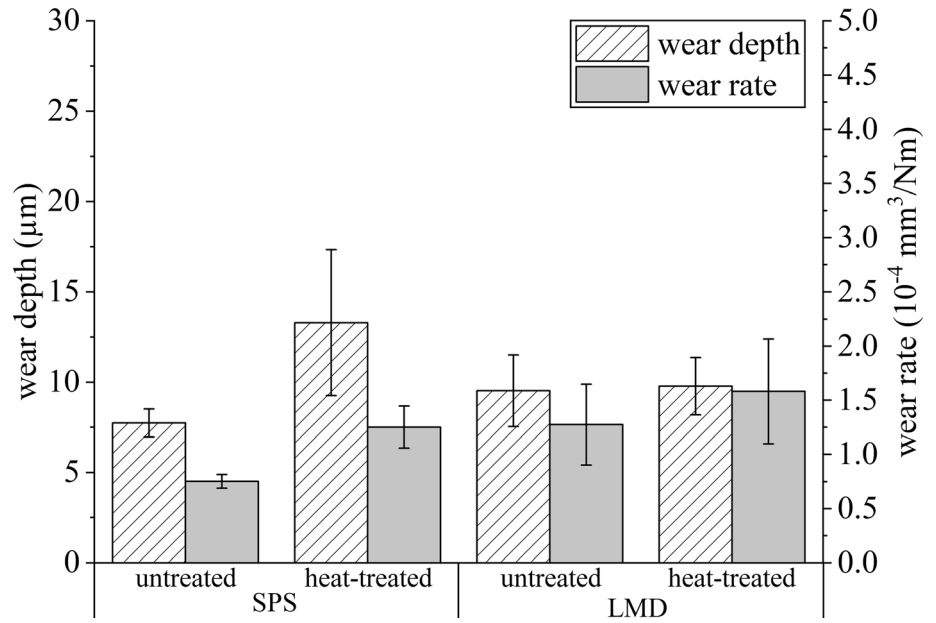

Fig. 8 SEM images (SE) of the worn surface after ball-on-disk test: (a) untreated and (b) heat-treated SPS bulk material as well as (c) untreated and (d) heat-treated LMD coating

removal due to the formation of wear debris as additional wear bodies during the reciprocating wear test are the reason.

Finally, scratch resistances of the SPS bulk materials and LMD coatings were determined by conducting scratch tests under constant load (Fig. 12). It can be seen that the residual depth increases with higher loads. At a low load of

Fig. 9 Wear depth and wear rate (reciprocating wear test) of the SPS bulk material and LMD coating in the untreated and heat-treated state
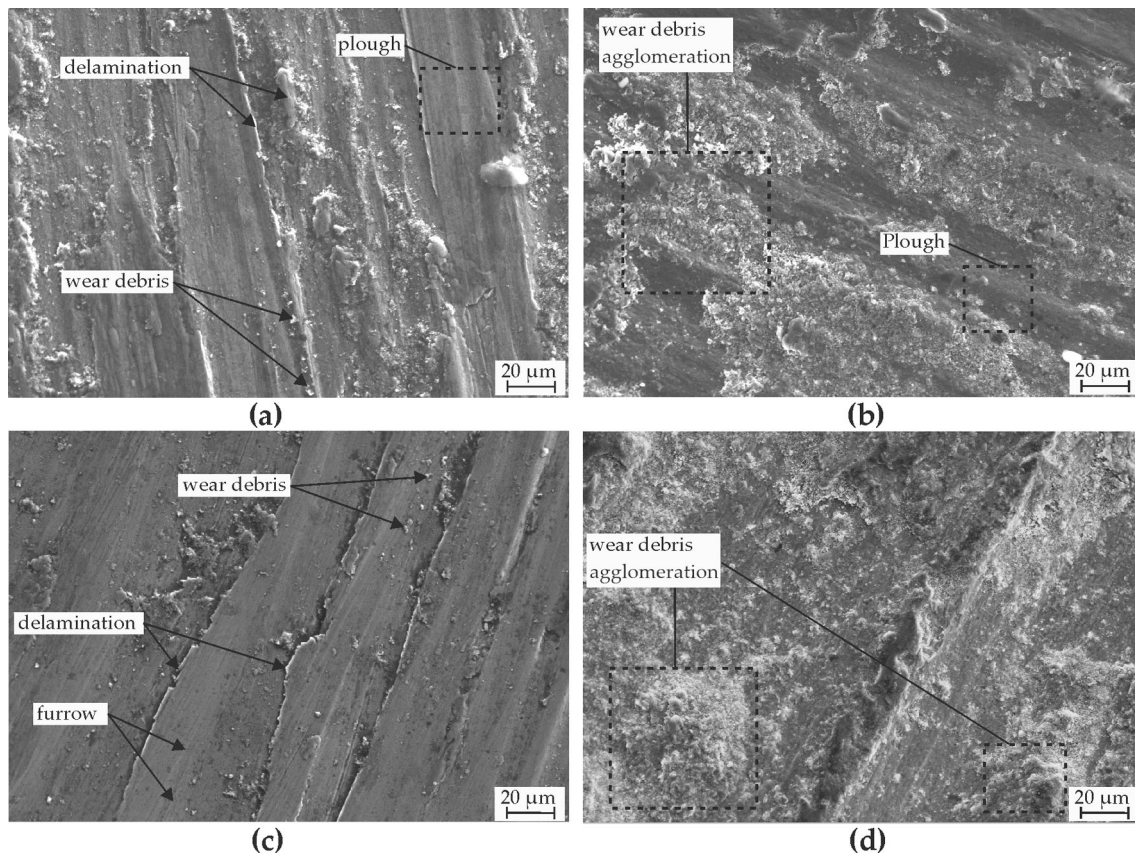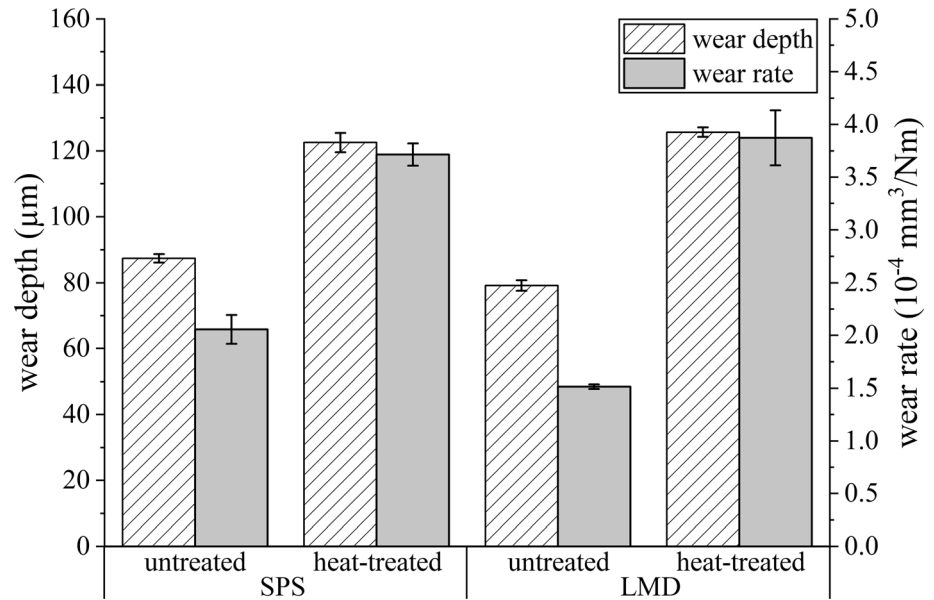

Fig. 10 SEM images (SE) of the worn surface after reciprocating wear test: (a) untreated and (b) heat-treated SPS bulk material as well as (c) untreated and (d) heat-treated LMD coating

50 N, the untreated LMD coating performs best. By homogenizing the SPS bulk material and LMD coating due to heat treatment, the wear depth doubles. With an increase of the scratch load up to 150 N, the untreated SPS bulk material exhibits the highest wear resistance. This is caused by the lower porosity as well as the ultrafine eutectic structure. In contrast, a brittle behavior of the untreated LMD coating and directional solidification could cause
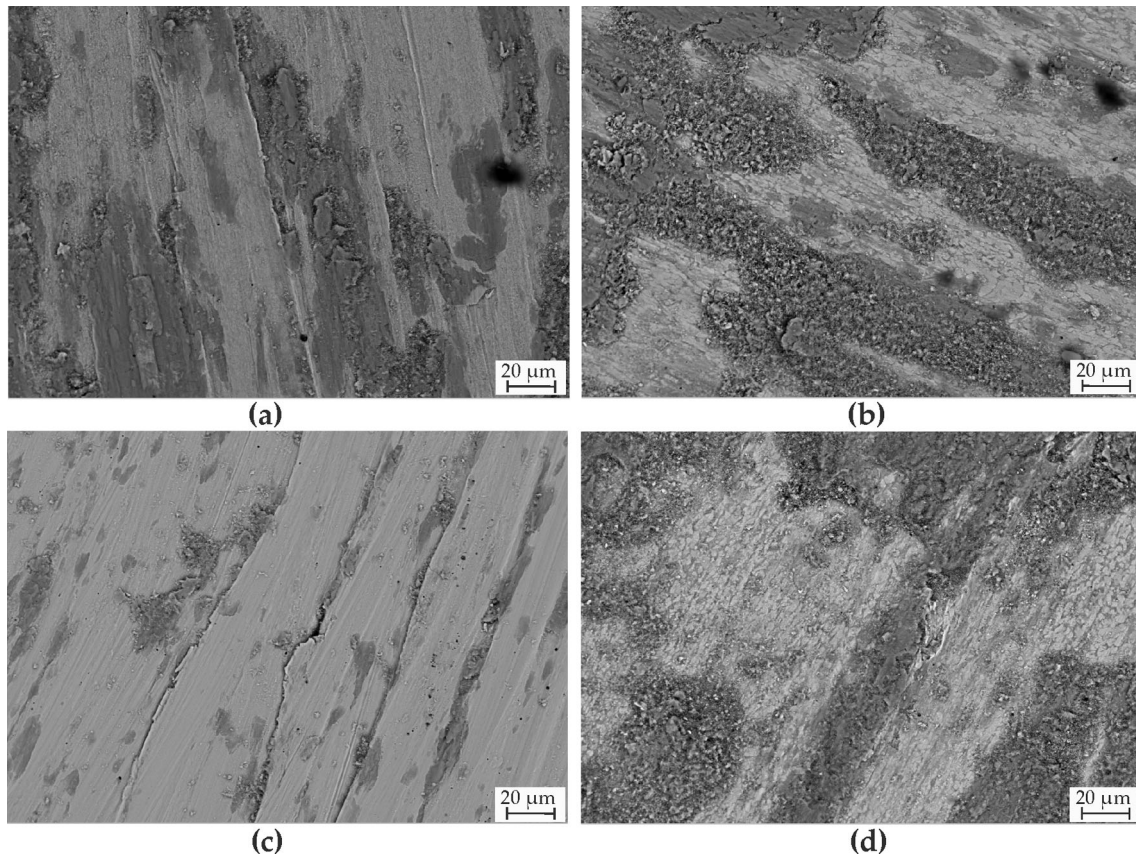
Fig. 11 SEM images (BSD) of the worn surface after reciprocating wear test: (a) untreated and (b) heat-treated SPS bulk material as well as (c) untreated and (d) heat-treated LMD coating
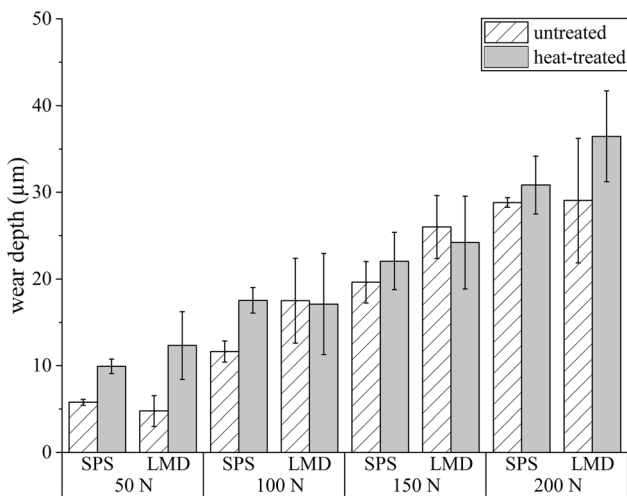

Fig. 12 Wear depth (scratch test) of the SPS bulk material and LMD coating in the untreated and heat-treated states

higher wear depths. Consequently, the heat-treated LMD coating with homogeneous and less pronounced directional solidified microstructure shows higher scratch resistance. At the maximum load of 200 N, the average wear depth for the untreated SPS bulk material and LMD coating is at a

similar level. The high standard deviation of the LMD coatings is due to its porosity. This indicates a lower surface quality than for the SPS bulk materials.

Corrosion Behavior

In addition to the wear tests, the corrosion resistance of the SPS bulk materials was recorded. Due to the increased number of cracks along the LMD coating, the substrate material influences their corrosion behavior. Thus, the results from the corrosion measurements for the LMD coatings are only of limited significance when compared to the SPS bulk materials.

Potentiodynamic polarization measurements in NaCl and H_2SO_4 electrolytes were conducted to detect the pitting and passivation behaviors. Typical potentiodynamic polarization curves for the SPS bulk materials are shown in Fig. 13. The values E_{corr} and i_{corr} listed in Table 8 were determined by evaluation of the potentiodynamic polarization curves. Due to the multiphase microstructure, varying contents of the FCC and HCP phases can be present within the corroded area. The individual measurements showed different mixed potentials, which increases

Fig. 13 Typical
potentiodynamic polarization
curves of the untreated and heat-
treated SPS bulk materials:
(a) 0.5 M NaCl electrolyte and
(b) 0.05 M H_2SO_4 electrolyte
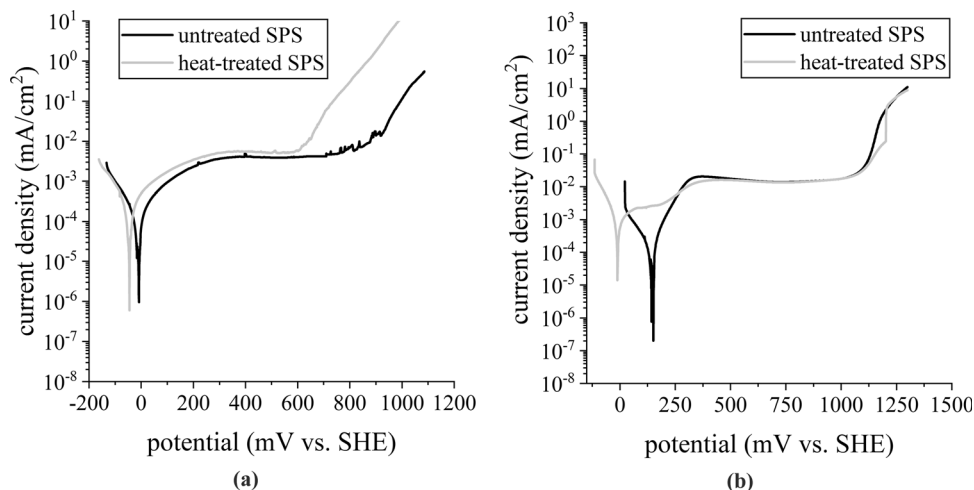
the standard deviations. Using 0.05 M H_2SO_4, it was observed that E_{corr} decreases significantly due to heat treatment. This indicates a less noble behavior due to the heat-treatment related segregation. The i_{corr} increases as a result. The depletion of the solid solution in Cr and especially Mo as a result of the heat treatment could be responsible. This indicates that the Mo and Cr depleted intermetallic phase preferentially dissolves in the electrolyte. In contrast, the untreated SPS bulk material with a higher Mo content within the solid solution exhibit an improved corrosion behavior. Löbel et al. (Ref 31) already detected the enhancement of the corrosion resistance by adding Mo. With homogenization, the Mo content in the solid solution decreases. Hence, the corrosion resistance is reduced. The heat-treated SPS bulk material easily passivates at around 100 mV vs. standard hydrogen electrode (SHE). At around 200 mV vs. SHE, the current density increases by a factor of about 5 to approx. 10^{-2} mA/cm² in a second passive region. The passivation potential of the untreated SPS bulk material is about 350-380 mV vs. SHE. For higher potentials, the current density decreases and reaches a value which is similar to one of the heat-treated SPS bulk material. This indicates the formation of a stable passive film on the surface for both states. The pitting potential is approx. 1100 mV vs. SHE for the untreated SPS bulk material. The heat-treated condition has a slightly lower pitting potential (approx. 20 mV lower).

In contrast in 0.5 M NaCl electrolyte, heat-treatment increased the E_{corr}, whereas similar i_{corr} values were detected for both conditions. This indicates that the natural passive layer in the electrolyte is similarly stable for both phases, the HCP and FCC. Despite Cr and Mo depletion of the FCC phase after the heat treatment, it remains stable. Thus, no significant change in i_{corr} occurs between the two states. Due to the low current density at a high polarization range, a passive behavior can be detected for both states.

The pitting resistance deteriorates due to the heat treatment (untreated 870 mV vs. SHE; heat-treated 610 mV vs. SHE). When comparing with the findings of Löbel et al. (Ref 32) on the HEA $Al_{0.3}CoCrFeNiMo_{0.2}$, the SPS bulk material reaches similar corrosion potentials and current density.

Measurements on the untreated LMD coatings with 0.5 M NaCl showed positive potentials of approx. 120 mV vs. SHE with a current density of approx. 0.5 µA/cm². In contrast, the untreated LMD coating exhibits a much higher potential of approx. 250 mV vs. SHE and a higher current density of approx. 1.8 µA/cm² by using H_2SO_4 electrolyte. Compared to thermally sprayed AlCrFeCoNi coatings with a potential of (-133 ± 26) mV vs. SHE (HVOF) and (-155 ± 13) mV vs. SHE (HVAF) in 0.5 M NaCl (Ref 47), the untreated and heat-treated SPS bulk materials and LMD coatings exhibit a nobler E_{corr}. This is due to the significantly higher Mo content. However, these values are influenced by the substrate due to cracks in the LMD coating, which also leads to large deviations even for identical samples.

Summary

By SPS and LMD, bulk materials and coatings of the metastable EHEA $Al_{0.3}CoCrFeNiMo_{0.75}$ were successfully produced. A heat treatment at 1100 °C for 12 h was conducted. Different production routes were used to identify the influence of heat treatment and cooling conditions on the microstructure and system properties. Accordingly, statements on the formation of metastable phases in coatings are possible. For the metastable EHEA $Al_{0.3}CoCrFeNiMo_{0.75}$, following findings can be made:

- The LMD process leads to an ultrafine-grained Widmanstätten structure consisting of a supersaturated solid solution FCC phase as well as a σ- and a µ-phase.

Table 8 Corrosion current density and corrosion potential of the SPS $Al_{0.3}CoCrFeNiMo_{0.75}$ bulk material

Condition	Electrolyte	E_{corr}, mV vs. SHE	i_{corr}, $\mu A/cm^2$
Untreated SPS	NaCl	-60 ± 50	$(2.6 \pm 1.6) \cdot 10^{-1}$
	H_2SO_4	162 ± 24	$(1.10 \pm 0.24) \cdot 10^{-1}$
Heat-treated SPS	NaCl	-18 ± 28	$(1.6 \pm 1.0) \cdot 10^{-1}$
	H_2SO_4	2 ± 19	$(20 \pm 5) \cdot 10^{-1}$

Furthermore, solidification vertical to the intermixing zone was determined for the LMD coating. The SPS bulk material showed a statistically orientated fine-lamellar structure defined by the microstructure of the powder.

- The ultrafine-grained Widmanstätten structure and the supersaturated solid solution of the untreated LMD coating was detected with the highest hardness and oscillating wear resistance.
- Under sliding wear conditions, the SPS bulk material exhibits the highest wear resistance.
- Potentiodynamic polarization measurements in H_2SO_4 electrolyte show a higher corrosion potential with significantly reduced corrosion current density for the untreated SPS bulk material compared to the heat-treated condition. Furthermore, a stable passive film is formed in the untreated SPS bulk material over a wide potential range.
- In NaCl solution, the corrosion potential as well as corrosion current density for both conditions are similar, whereas the pitting potential is considerably higher for the untreated SPS bulk material.

Conclusion

The present study demonstrates a microstructural evolution of the EHEA $Al_{0.3}CoCrFeNiMo_{0.75}$ influenced by the production route (cooling conditions) and subsequent heat treatment. This is accompanied by a change in hardness and tribological and corrosion properties. Following conclusions for the EHEA $Al_{0.3}CoCrFeNiMo_{0.75}$ can be drawn:

- Creation of tailored microstructures is possible by adjusted cooling conditions. However, the achievable cooling rates of the LMD process are not sufficiently high to sustain the metastable BCC phase present in the powder.
- Depending on the substrate and its thermal expansion coefficient, the higher cooling rates of the LMD process cause intense crack and pore formation. Thus, by further increase of the cooling rate, a deterioration of the overall properties of the coating is expected. Hence,

a crack-free production of the metastable BCC phase by using the LMD process is not possible.

- A pronounced intermixing zone in the proximity of the substrate influences the phases and the property profile. Hence, a minimum coating thickness of approx. 300 μm is required to reach the above-mentioned corrosion and wear properties.
- The ultrafine-grained Widmanstätten structure is suitable for the use under harsh oscillating-wear and corrosion conditions, whereas the ultrafine-lamellar structure produced by SPS is appropriate for sliding wear applications.
- A diffusion-related phase transformation is present in high temperature applications (> 1100 °C for extended periods). Therefore, a reduction in wear and corrosion resistance is expected.

In future studies, further corrosion tests with gel electrolytes have to be conducted for the LMD coatings to test the corrosion properties of the Widmanstätten structure independently of the substrate—despite the presence of cracks. Furthermore, different heat treatment parameters and cooling conditions have to be used to understand the phase formations and resulting properties of the EHEA $Al_{0.3}CoCrFeNiMo_{0.75}$ in more detail.

References

1. A. Meghwal, A. Anupam, B.S. Murty, C.C. Berndt, R.S. Kottada, and A.S.M. Ang, Thermal Spray High-Entropy Alloy Coatings: A Review, *J. Therm. Spray Tech.*, 2020, **29**(5), p 857–893.

2. M.C. Gao, J.-W. Yeh, P.K. Liaw, and Y. Zhang Eds., *High-Entropy Alloys: Fundamentals and Applications. Softcover reprint of the original*, 1st ed. Springer International Publishing, Cham, 2018

3. Y. Lu, Y. Dong, S. Guo, L. Jiang, H. Kang, T. Wang, B. Wen, Z. Wang, J. Jie, Z. Cao, H. Ruan,, and T. Li, A Promising New Class of High-Temperature Alloys: Eutectic High-Entropy Alloys, *Sci. Rep.*, 2015, **4**(1), p 6200.

4. J. Miao, H. Liang, A. Zhang, J. He, J. Meng, and Y. Lu, Tribological Behavior of an AlCoCrFeNi2.1 Eutectic High Entropy Alloy Sliding Against Different Counterfaces, *Tribol. Int.*, 2021, **153**, p 106599.

5. S. Shuang, Q. Yu, X. Gao, Q.F. He, J.Y. Zhang, S.Q. Shi, and Y. Yang, Tuning the Microstructure for Superb Corrosion Resistance in Eutectic High Entropy Alloy, *J. Mater. Sci. Technol.*, 2022, **109**, p 197–208.

6. T.S. Kumar, L. Chauhan, K. Chakravarthy, and A. Chelvane, The Improved Galvanic Corrosion Resistance of a Eutectic High Entropy Alloy through Heat Treatment, *J. Mater. Res.*, 2022, **37**(23), p 4211–4221.

7. X. Cao, C. Wu, Y. Liu, H. Peng, and X. Su, Eutectic Reaction and Microstructure Stability in $CoCrFeNiNb_X$ High-Entropy Alloys, *Metals*, 2022, **12**(5), p 756.

8. T. Nagase, M. Takemura, M. Matsumuro, and T. Maruyama, Solidification Microstructure of $AlCoCrFeNi_{2.1}$ Eutectic High Entropy Alloy Ingots, *Mater. Trans.*, 2018, **59**(2), p 255–264.

9. A. Nassar, A. Mullis, R. Cochrane, Z. Aslam, S. Micklethwaite, and L. Cao, Rapid Solidification of $AlCoCrFeNi_{2.1}$ High-Entropy Alloy, *J. Alloys Compd.*, 2022, **900**, p 163350.

10. R.P. Todorov and Kh.G. Khristov, Widmanstatten Structure of Carbon Steels, *Met. Sci. Heat Treat.*, 2004, **46**(1/2), p 49–53.

11. C.-F. Lee and T.-T. Shun, Age Heat Treatment of $Al_{0.5}CoCrFe_{1.5}NiTi_{0.5}$ High-Entropy Alloy, *Metals*, 2021, **11**(1), p 91.

12. C. Chen, Y. Fan, W. Wang, H. Zhang, J. Hou, R. Wei, T. Zhang, T. Wang, M. Li, S. Guan, and F. Li, Synthesis of Ultrafine Dual-Phase Structure in $CrFeCoNiAl_{0.6}$ High Entropy Alloy via Solid-State Phase Transformation during Sub-Rapid Solidification, *J. Mater. Sci. Technol.*, 2022, **113**, p 253–260.

13. A. Zhang, J. Han, J. Meng, B. Su, and P. Li, Rapid Preparation of AlCoCrFeNi High Entropy Alloy by Spark Plasma Sintering from Elemental Powder Mixture, *Mater. Lett.*, 2016, **181**, p 82–85.

14. I. Moravcik, J. Cizek, P. Gavendova, S. Sheikh, S. Guo, and I. Dlouhy, Effect of Heat Treatment on Microstructure and Mechanical Properties of Spark Plasma Sintered $AlCoCrFeNiTi_{0.5}$ High Entropy Alloy, *Mater. Lett.*, 2016, **174**, p 53–56.

15. W. Ji, W. Wang, H. Wang, J. Zhang, Y. Wang, F. Zhang, and Z. Fu, Alloying Behavior and Novel Properties of CoCrFeNiMn High-Entropy Alloy Fabricated by Mechanical Alloying and Spark Plasma Sintering, *Intermetallics*, 2015, **56**, p 24–27.

16. I. Moravcik, J. Cizek, J. Zapletal, Z. Kovacova, J. Vesely, P. Minarik, M. Kitzmantel, E. Neubauer, and I. Dlouhy, Microstructure and Mechanical Properties of $Ni_{1.5}Co_{1.5}CrFeTi_{0.5}$ High Entropy Alloy Fabricated by Mechanical Alloying and Spark Plasma Sintering, *Mater. Des.*, 2017, **119**, p 141–150.

17. S. Riva, S.G.R. Brown, N.P. Lavery, A. Tudball,, and K.V. Yusenko, Spark Plasma Sintering of High Entropy Alloys, *Spark Plasma Sintering of Materials*, P. Cavaliere, Ed., (Cham), Springer International Publishing, 2019, p 517-538, https://doi.org/10.1007/978-3-030-05327-7_18

18. L. Wang, X. Wu, C. Yao, J. Shen, Y. Zhang, Y. Ge, and G. Zhang, Microstructural Stability of As-Cast and Directionally Solidified $AlCoCrFeNi_{2.1}$ Eutectic High-Entropy Alloys at Elevated Temperatures, *Metall. Mater. Trans. A*, 2020, **51**(11), p 5781–5789.

19. W. Pan, P. Fu, Z. Li, H. Chen, Q. Tang, P. Dai, C. Liu, and L. Lin, Microstructure and Mechanical Properties of $AlCoCrFeNi_{2.1}$ Eutectic High-Entropy Alloy Synthesized by Spark Plasma Sintering of Gas-Atomized Powder, *Intermetallics*, 2022, **144**, p 107523.

20. B. Preuß, T. Lindner, T. Uhlig, G. Wagner, and T. Lampke, Niobium and Molybdenum as Alloying Constituents in $Al_{0.3}CoCrFeNi$ to Develop Eutectic High-Entropy Alloys for HVOF Spraying, *J Therm Spray Tech*, 2022 https://doi.org/10.1007/s11666-022-01417-w

21. L.-M. Rymer, T. Lindner, and T. Lampke, Nb and Mo Influencing the High-Temperature Wear Behavior of HVOF-Sprayed High-Entropy Alloy Coatings, *Coatings*, 2022, **13**(1), p 9.

22. M. Zhong and W. Liu, Laser Surface Cladding: The State of the Art and Challenges, *Proc. Inst. Mech. Eng. C J. Mech. Eng. Sci.*, 2010, **224**(5), p 1041–1060.

23. N. Shamsaei, A. Yadollahi, L. Bian, and S.M. Thompson, An Overview of Direct Laser Deposition for Additive Manufacturing; Part II: Mechanical Behavior, Process Parameter Optimization and Control, *Addit. Manuf.*, 2015, **8**, p 12–35.

24. W. Yuan, R. Li, Z. Chen, J. Gu, and Y. Tian, A Comparative Study on Microstructure and Properties of Traditional Laser Cladding and High-Speed Laser Cladding of Ni45 Alloy Coatings, *Surf. Coat. Technol.*, 2021, **405**, p 126582.

25. L. Huang, Y. Sun, N. Chen, H. Luan, G. Le, X. Liu, Y. Ji, Y. Lu, P.K. Liaw, X. Yang, Y. Zhou, and J. Li, Simultaneously Enhanced Strength-Ductility of $AlCoCrFeNi_{2.1}$ Eutectic High-Entropy Alloy via Additive Manufacturing, *Mater. Sci. Eng. A*, 2022, **830**, p 142327.

26. R. John, A. Karati, J. Joseph, D. Fabijanic, and B.S. Murty, Microstructure and Mechanical Properties of a High Entropy Alloy with a Eutectic Composition ($AlCoCrFeNi_{2.1}$) Synthesized by Mechanical Alloying and Spark Plasma Sintering, *J. Alloys Compd.*, 2020, **835**, p 155424.

27. L. Jiang, Y. Lu, W. Wu, Z. Cao, and T. Li, Microstructure and Mechanical Properties of a $CoFeNi_2V_{0.5}Nb_{0.75}$ Eutectic High Entropy Alloy in As-Cast and Heat-Treated Conditions, *J. Mater. Sci. Technol.*, 2016, **32**(3), p 245–250.

28. B. Preuß, T. Lindner, T. Uhlig, J.E. Tapia Cabrera, H. Schwarz, G. Wagner, T. Seyller, and T. Lampke, Microstructure Evolution and Wear Resistance of the Eutectic High-Entropy Alloy $Al_{0.3}CoCrFeNiNb_{0.5}$ Produced by Laser Metal Deposition, *Coatings*, 2023, **13**(3), p 585.

29. F. Kafexhiu, B. Podgornik, and D. Feizpour, Tribological Behavior of As-Cast and Aged $AlCoCrFeNi_{2.1}$ CCA, *Metals*, 2020, **10**(2), p 208.

30. Y.Y. Chen, U.T. Hong, H.C. Shih, J.W. Yeh, and T. Duval, Electrochemical Kinetics of the High Entropy Alloys in Aqueous Environments—a Comparison with Type 304 Stainless Steel, *Corros. Sci.*, 2005, **47**(11), p 2679–2699.

31. Y.L. Chou, J.W. Yeh, and H.C. Shih, The Effect of Molybdenum on the Corrosion Behavior of the High-Entropy Alloys $Co_{1.5}CrFeNi_{1.5}Ti_{0.5}MoX$ in Aqueous Environments, *Corros. Sci.*, 2010, **52**(8), p 2571–2581.

32. M. Löbel, T. Lindner, M. Grimm, L.-M. Rymer, and T. Lampke, Influence of Aluminum and Molybdenum on the Microstructure

and Corrosion Behavior of Thermally Sprayed High-Entropy Alloy Coatings, *J. Therm. Spray Tech.*, 2021 https://doi.org/10.1007/s11666-021-01297-6

33. Y. Liu, Y. Xie, S. Cui, Y. Yi, X. Xing, X. Wang, and W. Li, Effect of Mo Element on the Mechanical Properties and Tribological Responses of CoCrFeNiMo$_X$ High-Entropy Alloys, *Metals*, 2021, **11**(3), p 486.

34. T.-T. Shun, L.-Y. Chang, and M.-H. Shiu, Microstructure and Mechanical Properties of Multiprincipal Component CoCrFeNiMo$_X$ Alloys, *Mater Charact*, 2012, **70**, p 63–67.

35. C.-Y. Hsu, T.-S. Sheu, J.-W. Yeh, and S.-K. Chen, Effect of Iron Content on Wear Behavior of AlCoCrFeXMo$_{0.5}$Ni High-Entropy Alloys, *Wear*, 2010, **268**(5–6), p 653–659.

36. Q. Wu, Z. Wang, F. He, J. Li, and J. Wang, Revealing the Selection of σ and μ Phases in CoCrFeNiMo$_X$ High Entropy Alloys by CALPHAD, *J. Phase Equilib. Diffus.*, 2018, **39**(4), p 446–453.

37. F. Shen, W. Tao, L. Li, Y. Zhou, W. Wang, and S. Wang, Effect of Microstructure on the Corrosion Resistance of Coatings by Extreme High Speed Laser Cladding, *Appl. Surf. Sci.*, 2020, **517**, p 146085.

38. T. Liao, Z. Wang, X. Wu, Q. Liu, Y. Guo, K. Ding, and X. Shang, Effect of V on microstructure, wear and corrosion properties in AlCoCrMoVx high entropy alloy coatings by laser cladding, *J. Mater. Res. Technol.*, 2023, **23**, p 4420–4431.

39. A. Asabre, A. Kostka, O. Stryzhyboroda, J. Pfetzing-Micklich, U. Hecht, and G. Laplanche, Effect of Al, Ti and C Additions on Widmanstätten Microstructures and Mechanical Properties of Cast Al$_{0.6}$CoCrFeNi Compositionally Complex Alloys, *Mater. Design*, 2019, **184**, p 108201.

40. Y. Palguna and R. Korla, Comparative Study of Microstructure and Mechanical Properties of Thermo-Mechanically Processed Al$_{(0.2, 0.5)}$CoCrFeNiMo$_{0.5}$ High-Entropy Alloys, *Philos. Magaz. Lett.*, 2023, **103**(1), p 2170490.

41. W.-R. Wang, W.-L. Wang, S.-C. Wang, Y.-C. Tsai, C.-H. Lai, and J.-W. Yeh, Effects of Al Addition on the Microstructure and Mechanical Property of Al$_X$CoCrFeNi High-Entropy Alloys, *Intermetallics*, 2012, **26**, p 44–51.

42. X. Wen, X. Cui, G. Jin, Y. Liu, Y. Zhang, and Y. Fang, In-Situ Synthesis of Nano-Lamellar Ni$_{1.5}$CrCoFe$_{0.5}$Mo$_{0.1}$NbX Eutectic High-Entropy Alloy Coatings by Laser Cladding: Alloy Design and Microstructure Evolution, *Surface Coat. Technol.*, 2021, **405**, p 126728.

43. A. Munitz, S. Salhov, S. Hayun, and N. Frage, Heat Treatment Impacts the Micro-Structure and Mechanical Properties of AlCoCrFeNi High Entropy Alloy, *J. Alloy. Compd.*, 2016, **683**, p 221–230.

44. C. Nagarjuna, K. Yong Jeong, Y. Lee, S. Min Woo, S. Ig Hong, H. Seop Kim, and S.-J. Hong, Strengthening the Mechanical Properties and Wear Resistance of CoCrFeMnNi High Entropy Alloy Fabricated by Powder Metallurgy, *Adv. Powder Technol.*, 2022, **33**(4), p 103519.

45. L.M. Rymer, T. Lindner, and T. Lampke, Enhanced High-Temperature Wear Behavior of High-Speed Laser Metal Deposited Al$_{0.3}$CrFeCoNi Coatings Alloyed with Nb and Mo, *Surface Coat. Technol.*, 2023, **470**, p 129832.

46. J. Lakshmipathy and B. Kulendran, Reciprocating Wear Behavior of 7075Al/SiC and 6061Al/Al$_2$O$_3$ Composites: A Study of Effect of Reinforcement, *Stroke Load*, 2014, **36**(2), p 117–126.

47. M. Löbel, T. Lindner, T. Mehner, L.-M. Rymer, S. Björklund, S. Joshi, and T. Lampke, Microstructure and Corrosion Properties of AlCrFeCoNi High-Entropy Alloy Coatings Prepared by HVAF and HVOF, *J. Therm. Spray Tech.*, 2022, **31**(1–2), p 247–255.